

BRILLOUIN SPECTROSCOPIC STUDIES
OF THE ORIENTATIONALLY DISORDERED
PHASE OF C_2F_6

CENTRE FOR NEWFOUNDLAND STUDIES

**TOTAL OF 10 PAGES ONLY
MAY BE XEROXED**

(Without Author's Permission)

GORDON TODD ANDREWS, B.Sc.(Hons.)



BRILLOUIN SPECTROSCOPIC STUDIES
OF THE ORIENTATIONALLY DISORDERED PHASE OF C_2F_6

By

©Gordon Todd Andrews

B. Sc. (Hons.), Memorial University of Newfoundland

A THESIS SUBMITTED TO THE SCHOOL OF GRADUATE
STUDIES IN PARTIAL FULFILLMENT OF THE
REQUIREMENTS FOR THE DEGREE OF
MASTER OF SCIENCE

DEPARTMENT OF PHYSICS
MEMORIAL UNIVERSITY OF NEWFOUNDLAND
JULY 1992

ST. JOHN'S

NEWFOUNDLAND



National Library
of Canada

Acquisitions and
Bibliographic Services Branch

395 Wellington Street
Ottawa, Ontario
K1A 0N4

Bibliothèque nationale
du Canada

Direction des acquisitions et
des services bibliographiques

395, rue Wellington
Ottawa (Ontario)
K1A 0N4

ISBN 0-315-78107-6

La loi sur l'accès à l'information

The author has granted an irrevocable non-exclusive licence allowing the National Library of Canada to reproduce, loan, distribute or sell copies of his/her thesis by any means and in any form or format, making this thesis available to interested persons.

L'auteur a accordé une licence irrévocable et non exclusive permettant à la Bibliothèque nationale du Canada de reproduire, prêter, distribuer ou vendre des copies de sa thèse de quelque manière et sous quelque forme que ce soit pour mettre des exemplaires de cette thèse à la disposition des personnes intéressées.

The author retains ownership of the copyright in his/her thesis. Neither the thesis nor substantial extracts from it may be printed or otherwise reproduced without his/her permission.

L'auteur conserve la propriété du droit d'auteur qui protège sa thèse. Ni la thèse ni des extraits substantiels de celle-ci ne doivent être imprimés ou autrement reproduits sans son autorisation.

ISBN 0-315-78107-6

Canada

Abstract

The elastic constants and elasto-optic coefficient ratios of the orientationally disordered β -phase of C_2F_6 have been determined using the technique of high resolution Brillouin spectroscopy. Just below the triple point, at 169 K, the values of the elastic constants (in units of *kbar*) are:

$$C_{11} = 26.99 \pm 0.10,$$

$$C_{12} = 19.32 \pm 0.10,$$

$$C_{44} = 4.44 \pm 0.04.$$

The elasto-optic coefficient ratios at 169 K are:

$$p_{12}/p_{11} = 1.09 \pm 0.09,$$

$$p_{44}/p_{11} = 0.12 \pm 0.01.$$

The temperature dependence of all three elastic constants was also determined over the range 169 K to 144 K. C_{11} and C_{12} appear to have linear temperature dependences, with $\Delta C_{11}/\Delta T = -0.335 \pm 0.010$ *kbar/K*, and $\Delta C_{12}/\Delta T = -0.236 \pm 0.010$ *kbar/K*. C_{44} , however, appears to be independent of temperature in this range, with $\Delta C_{44}/\Delta T = 0.005 \pm 0.011$ *kbar/K*.

Values of the ratios of acoustic velocities in high symmetry directions in the crystal indicate near perfect elastic isotropy and that moderately strong rotation-translation coupling is present in β - C_2F_6 . The extent of the coupling is of the order of that observed in plastic $(CH_2CN)_2$. This is in contrast to the structurally similar orientationally disordered phase of SF_6 , which behaves elastically like a rare gas solid.

Acknowledgements

I wish to thank my supervisors, Dr. H. Kiefte and Dr. M.J. Clouter, for sharing with me their expertise in the field of light scattering and for their skilful direction of my research.

I would like to express my gratitude to Mr. R. Baranowski for his help in the typesetting of this thesis, Mr. W. Holly for providing a continuous supply of liquid nitrogen, Mr. R. Guest for the drafting of several figures and Mr. R. Bradley for prints of several photographs.

I would also like to thank my family who have always encouraged me to pursue my interests.

While engaged in this work I was supported by a Memorial University Graduate Fellowship which I gratefully acknowledge.

Table of Contents

Abstract	ii
Acknowledgements	iii
List of Tables	vi
List of Figures	vii
1 Introduction	1
1.1 Orientational Disorder and Rotation-Translation Coupling in Molecular Solids	1
1.2 Structure and Phases of C_2F_6	5
1.3 Disorder and Dynamics of C_2F_6	6
2 Theory	10
2.1 Brillouin Scattering	10
2.2 Acoustic Waves and Elastic Constants	12
2.3 Elasto-optic Coefficients of Cubic Crystals	15
2.4 Derived Quantities	17
3 Experimental	18
3.1 Experimental Setup	18
3.2 Cryostat	20
3.3 Temperature Sensing and Control	22

3.4	Gas Handling System	23
3.5	Growth of Crystals	24
3.6	Crystal Orientation and X-ray Apparatus	25
3.7	Laser	27
3.8	Fabry-Perot Interferometer	27
3.9	Data Acquisition and Stabilization System	29
3.10	Optical System Alignment	30
3.11	Brillouin Spectra	31
4	Results	35
4.1	Brillouin Shifts and Intensities	35
4.2	Elastic Constants	38
4.3	Elasto-optic Coefficients	43
4.4	Derived Quantities	44
5	Discussion	45
5.1	Results for C_2F_6	45
5.2	Comparison to other Orientationally Disordered Molecular Solids	46
5.3	Conclusion	51
	References	53

List of Tables

1.1	Ratios of acoustic velocities in high symmetry directions for various molecular solids near their triple points.	3
4.1	Brillouin scattering data for β - C_2F_6 at 169 K.	37
4.2	Brillouin scattering data for β - C_2F_6 at 160 K.	38
4.3	Brillouin scattering data for β - C_2F_6 at 144 K.	38
4.4	Temperature dependent data for β - C_2F_6	40
4.5	Elasto-optic ratios and coefficients for β - C_2F_6	43
4.6	Adiabatic bulk modulus and anisotropy factor for β - C_2F_6	44
5.1	Temperature dependence of ratios of acoustic velocities in high symmetry directions for β - C_2F_6	46
5.2	Ratios of acoustic velocities in high symmetry directions for several molecular solids near their triple points.	47
5.3	Elastic constants of Xe , SF_6 , $(CH_2CN)_2$ and C_2F_6 near their triple points.	51

List of Figures

1.1	The near octahedral molecular structure of C_2F_6	7
2.1	Brillouin scattering geometry.	11
3.1	The complete experimental setup for Brillouin scattering experiments on β - C_2F_6	19
3.2	The cryostat tail section.	21
3.3	Laue diffraction photograph of crystal #3.	26
3.4	A Brillouin stick spectrum showing the Rayleigh peaks (R) and the various Brillouin components (T_1 , T_2 and L).	34
4.1	A typical Brillouin spectrum of β - C_2F_6	36
4.2	Adiabatic elastic constants of β - C_2F_6 as a function of temperature. The uncertainties are approximately the size of the symbols.	42

Chapter 1

Introduction

1.1 Orientational Disorder and Rotation-Translation Coupling in Molecular Solids

In the past few years there has been much theoretical and experimental interest in orientationally disordered solids [1], [2]. Such solids are characterized by long range translational order (although individual molecular center of mass displacements about fixed lattice sites may be large) and molecular orientational disorder. Of particular interest in these solids is the coupling between the rotational and translational molecular motions. This coupling is a well known phenomenon in molecular liquids [3], but in molecular solids its effects are only recently being understood. Rotation-translation coupling, as it is known, may be thought of as arising from the change in orientational potential due to the local strain induced by a phonon [4] or, alternatively, as a coupling between the hydrodynamic anisotropy density and the strain field [5] or simply, the interaction between the rotational and translational degrees of freedom. Qualitatively, it is easy to imagine that any change in molecular rotational motion will perturb and, in many cases, dampen (or soften) the translational motion of the molecules. Consequently, this coupling is often strong enough to alter the nature of the collective excitations of the solid.

An extensive review of the literature on rotation-translation coupling may be found in reference [6]. Many techniques have been used to study rotation-translation in molecular

solids. The most common include molecular dynamics computer simulations and the technique of neutron scattering. In addition, however, light scattering has also been used to investigate this phenomenon in orientationally disordered solids. Brillouin scattering experiments on the disordered phases of SF_6 [7], CBr_4 [8], CCl_4 [9], cyclooctane and O_2 [10] in this laboratory as well as the pioneering work of Rand and Stoicheff on CH_4 and CD_4 [11] have contributed significantly to an understanding of this coupling in these solids.

In orientationally disordered solids, rotation-translation coupling may be observed as a decrease in (or softening of) acoustic phonon frequencies. The transverse acoustic phonons are especially susceptible to coupling to rotational motions. A quantitative measure of the extent of this coupling is provided by the density-independent ratios of acoustic velocities in high symmetry directions in the crystal, namely V_L/V_{T_1} and V_L/V_{T_2} (where L , T_1 and T_2 correspond to the longitudinal, the slow and the fast transverse acoustic modes, respectively), which may be calculated once the elastic constants of the solid have been determined [11]. These acoustic velocity ratios for various molecular crystals are given in Table 1.1, along with those for the rare gas solids. The values for the rare gas solids serve as a zero rotation-translation coupling reference because they are monatomic and thus independent of rotations. Therefore, ratios for a simple molecular solid (of cubic symmetry) which are significantly greater than the corresponding ratios for the rare gas solids could indicate that some degree of rotation-translation coupling exists.

The first Brillouin scattering evidence of acoustic mode softening was noted by Rand and Stoicheff [11] who measured an anomalously large value of V_L/V_{T_1} in the $\langle 110 \rangle$

direction in both CH_4 and CD_4 (see Table 1.1) and consequently attributed it to rotation-translation coupling. The theoretical calculations of Wonneberger and Hüller [12], which assumed a Leonard-Jones type interaction between molecules, later confirmed the role of rotation-translation coupling in reducing transverse acoustic phonon frequencies in CD_4 . In addition, this theory also yielded values for the elastic constants and elastic anisotropy which were in good agreement with those obtained from experiment [15].

Table 1.1: Ratios of acoustic velocities in high symmetry directions for various molecular solids near their triple points.

SOLID	$\langle 100 \rangle$	$\langle 111 \rangle$	$\langle 110 \rangle$	$\langle 110 \rangle$
	$V_L/V_{T_2, T_1}$	$V_L/V_{T_2, T_1}$	V_L/V_{T_2}	V_L/V_{T_1}
Ne, Ar, Kr, Xe [13]	1.44	2.24	1.65	2.71
CH_4, CD_4 [11]	1.47	2.46	1.70	3.23
CBr_4 [8]	1.66	2.74	1.87	3.74
CCl_4 [9]	1.79	3.07	2.01	4.70
$(CH_2CN)_2$ [14]	2.79	2.60	2.76	2.54
C_8H_{16} (cyclooctane) [10]	3.49	3.35	3.48	3.29
O_2 [10]	3.07	3.09	3.07	3.10

This softening of transverse acoustic phonons has subsequently been observed in several orientationally disordered van der Waals solids. Brillouin scattering experiments on the orientationally disordered phase of CBr_4 [8] have found significantly softened transverse phonons in the $\langle 111 \rangle$ and especially the $\langle 110 \rangle$ direction near $q = 0$, indicative of rotation-translation coupling. Neutron scattering experiments on CBr_4 [16] also suggested a strong rotation-translation coupling near $q = 0$. These results were not consistent with molecular dynamics simulations of the orientationally disordered phase of CBr_4 [17] where no rotation-translation coupling was predicted in this region.

One of the most extreme examples, to date, of an orientationally disordered solid exhibiting softened transverse phonon frequencies, is the cubic phase Ia of CCl_4 . Light scattering experiments [9] on this phase yielded acoustic velocity ratios which were 40% and 70% higher than the corresponding ratios for the rare gas solids in the $\langle 111 \rangle$ and $\langle 110 \rangle$ directions, respectively. Rotation-translation coupling, in fact, is so strong in CCl_4 that it is believed to be responsible for the metastability of phase Ia. This metastability was also predicted in the molecular dynamics simulations of McDonald *et al.* [18] and was attributed to a strong damping of slow $\langle 110 \rangle$ transverse phonons.

Brillouin scattering investigations of the orientationally disordered phases of cyclooctane [10], O_2 [10], and light scattering experiments on $(CH_2CN)_2$ [19] have found near perfect elastic isotropy near their respective triple points and high ratios of acoustic velocities in all three high symmetry directions $\langle 100 \rangle$, $\langle 111 \rangle$ and $\langle 110 \rangle$. In the case of cyclooctane and O_2 , the above features were consistent with strong rotation-translation coupling. A theory developed by Courtens [5] for $(CH_2CN)_2$, which included coupling of molecular reorientational motion to transverse acoustic phonons, was in excellent agreement with the experimental results.

The softening of acoustic phonon frequencies may also result in decreased mechanical stability of the solid and a corresponding decrease in the shear elastic constants as an order-disorder phase transition is approached. The relevant theory for ionic molecular solids has been developed mainly by Michel and Naudts [20], [21], [22]. The intermolecular interaction is described by a Born-Mayer repulsive overlap potential and the Hamiltonian includes both translational and rotational degrees of freedom as well as a coupling between these motions. Here, a vanishing value of shear elastic constant C_{44}

was predicted near the structural phase transitions of these solids. This was in agreement with both neutron [23] and Brillouin scattering [24] studies as well as ultrasonic measurements [25]. In particular, softening of elastic constant C_{44} was observed in Brillouin [26] and inelastic neutron scattering [23] of KCN as its phase transition was approached from above.

1.2 Structure and Phases of C_2F_6

The hexasubstituted ethanes (C_2X_6 , where X is a halogen) comprise a class of solids all of which exhibit an orientationally disordered plastic phase between their melting points and low temperature phases. One of the members of this class is the high temperature phase of hexafluoroethane (C_2F_6).

The orientationally disordered β -phase of C_2F_6 exists below the triple point of 173.1 K [27]. The crystal structure is body-centered cubic with molecules of symmetry $\bar{3}m$ occupying sites of symmetry $m\bar{3}m$ in the cubic I lattice [28]. The existence of a transition to a low temperature α -phase at 104 K was indicated by heat capacity data [27] as well as measurements of NMR linewidth [29] and the IR vibrational spectra [30]. X-ray diffraction data at 83 K [30] indicate that the low temperature phase has monoclinic structure with space group $P2_1/m$. The X-ray diffraction results also suggest that there is disorder in the α -phase of the statistical type since only a few discrete diffraction spots were observed. This was substantiated by Koide *et al.* [31] who also suggested that there remains disorder concerning molecular orientation in the low temperature phase. Neutron diffraction experiments conducted by Powell *et al.* [28], however, show that powder profiles obtained at 95 K and 110 K are qualitatively similar and that both can

be indexed on the basis of a body-centered cubic structure. The low temperature profiles cannot be indexed on the basis of the monoclinic space group suggested by the X-ray studies. In addition, they found that a sluggish structural transition begins at 70 K and persists to 40 K such that both α and β phases coexist in this temperature range.

More recent neutron scattering experiments [32] indicate that a structural phase transition does occur between 91 K and 117 K. The low temperature data are currently being analyzed in an effort to determine the structure of the low temperature α -phase. There is clearly still some confusion about the phase transition temperature(s).

1.3 Disorder and Dynamics of C_2F_6

According to molecular dynamics simulations calculations, the origin of the disorder in β - C_2F_6 is twofold [33], [34]. The molecular symmetry is lower than the site symmetry which leads to statistical disorder in the orientations of the $C - C$ bonds. Since, however, the F_6 framework is nearly octahedral, the molecular symmetry is almost that of the site, and preliminary simulations of different models of C_2F_6 [33], [34] indicate that orientational frustration exists as in SF_6 [35], [36], [37]. The molecular structure of C_2F_6 is shown in Figure 1.1. In SF_6 , when the $S - F$ bonds are aligned along the cubic axes, the nearest neighbour interactions are attractive while the next nearest neighbour interactions are repulsive. This gives rise to competing intermolecular orientational interactions known as orientational frustration. The simulations suggest that orientational frustration is a significant feature in C_2F_6 and that many properties of the orientationally disordered phase are related to the dynamics of the approximate F_6 octahedra (rather than the disorder of the $C - C$ bonds) and are thus very similar to the corresponding properties of SF_6 .

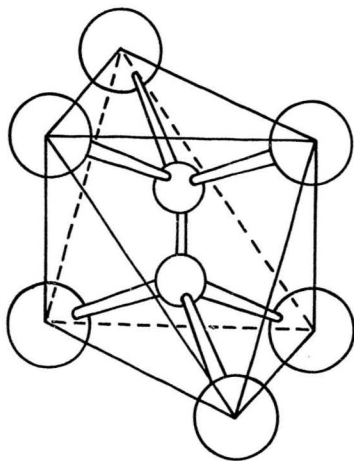


Figure 1.1: The near octahedral molecular structure of C_2F_6 .

Information concerning the single molecule motions in C_2F_6 has been obtained from the $C - F$ bond orientation distribution function determined by Powell *et al.* [28] at temperatures of 110 K and 95 K . This function indicates that although the fluorines are predominantly localized on the crystal axes, the distribution about these directions is very broad with a significant probability for the fluorines to be off axis. This distribution is qualitatively similar to that for SF_6 [38], which also exhibits broad maxima in the $\langle 100 \rangle$ directions. In the case of SF_6 at 96.5 K , the overall form of the bond orientation distribution function was attributed to large amplitude molecular librations about the cubic axes and substantial thermal reorientation. This may also be the case for C_2F_6 although motions more akin to rotational diffusion and/or low frequency reorientation have been suggested [29].

Molecular dynamics simulations also predict that the collective dynamics of C_2F_6 are very similar to those of plastic SF_6 [33], [34]. In particular, it is suggested that rotation-translation coupling in C_2F_6 will be strongest at $q = 0$ and drop to zero at the Brillouin zone boundary, parallelling the simulation results for SF_6 . Neutron diffraction experiments have shown that correlations between translational and rotational displacements in C_2F_6 are important [28]. Brillouin scattering experiments on SF_6 [7], however, show no (anomalous mode softening) evidence for strong rotation-translation coupling near $q = 0$.

It has been suggested by Koide *et al.* [31] that disorder can be acquired at the $\alpha \rightarrow \beta$ phase transition by internal rotation of one CF_3 group with respect to the other. They also state that in the high temperature phase the molecular axis (the central $C - C$ bond) runs parallel to the four body-diagonals in a random fashion and that the internal

rotation about the molecular axis and overall molecular rotation around the molecular axis begin to be fully excited. In the low temperature phase these motions are essentially frozen-in [31].

In order to examine the rotation-translation coupling mechanism in C_2F_6 and, in particular, to make a quantitative comparison to SF_6 , it is important that its elastic constants be determined. This has been done, in the present work, using the technique of high resolution Brillouin spectroscopy. Knowledge of the elastic constants allows for calculation of the density-independent ratios of acoustic velocities in high symmetry directions in the crystal. Comparison of these ratios for C_2F_6 with those of other orientationally disordered solids (in particular SF_6) provides information concerning the nature and extent of the rotation-translation coupling effect in β - C_2F_6 .

Chapter 2

Theory

2.1 Brillouin Scattering

It is well known that at temperatures greater than absolute zero the molecules in a crystal are in constant thermal motion. Collectively, these motions result in propagating lattice waves which, for wavelengths much greater than the unit cell side, are acoustic modes. The inelastic scattering of light by such thermally generated waves is known as Brillouin scattering.

The theory of Brillouin scattering in cubic crystals has been discussed in detail by Benedek and Fritsch [39]. They have shown that the frequency of the scattered light, ω_s , is shifted from that of the incident light, ω_i , according to

$$\omega_s = \omega_i \pm \omega_\mu, \quad (2.1)$$

where the $\omega_\mu = \omega_\mu(\vec{q})$ are the angular frequencies of the three acoustic modes with wavevector \vec{q} and different polarizations corresponding to three modes $\mu = L, T_1, T_2$.

For long wavelength acoustic modes, ω_μ is linear in q to a very good approximation. The dispersion relation is then

$$\omega_\mu = V_\mu q, \quad (2.2)$$

where V_μ is the magnitude of the velocity of the μ th mode in the \vec{q} direction. In the scattering process there is very little difference between the magnitude of the wavevector of the incident light, k_i and that of the scattered light, k_s . This is because the phonon (acoustic wave) energy is much less than that of the photon. Hence the wavevector

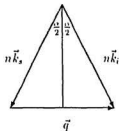


Figure 2.1: Brillouin scattering geometry.

triangle in Figure 2.1 is nearly isosceles and it is evident that

$$q = 2n k_i \sin\left(\frac{\alpha}{2}\right), \quad (2.3)$$

where n is the index of refraction of the medium being probed and α is the scattering angle.

Substitution of equations (2.2) and (2.3) into equation (2.1) then yields

$$\omega_s = \omega_i \pm 2\frac{n}{c} V_\mu \omega_i \sin\left(\frac{\alpha}{2}\right), \quad (2.4)$$

where k_i has been replaced by ω_i/c and c is the speed of light. Equation (2.1) is the well

known Brillouin equation.

Consequently, for single crystals, three Brillouin components corresponding to $\mu = L$ (quasilongitudinal), T_1 (slow quasitransverse), and T_2 (fast quasitransverse) are generally expected. They are observed as up and downshifted peaks located symmetrically about the Rayleigh peak at the incident laser frequency.

2.2 Acoustic Waves and Elastic Constants

The acoustic waves which propagate in crystalline solids have wavelengths much greater than the intermolecular spacings and therefore, in describing the motion of these waves, the crystal may be treated as an elastic continuum. Accordingly, the equations of motion of these waves are [40]

$$\rho \ddot{u}_i = C_{ijkl} \frac{\partial^2 u_l}{\partial x_j \partial x_k}, \quad (2.5)$$

where ρ is the density, \vec{u} is the displacement vector, $\vec{r} = x_i \hat{e}_i$ is the position vector and the C_{ijkl} are the elastic constants. The C_{ijkl} form a tensor of rank four. Symmetry properties of the tensor reduce the number of independent elements from 81 to 21. The tensor may then be written in matrix form by reducing the number of subscripts from 4 to 2 using the standard notation of Voigt. In the case of a system with cubic symmetry, such as the β -phase of hexafluoroethane, the high symmetry of the lattice further reduces the number of elastic constants to three, namely C_{11} , C_{12} and C_{44} , and the matrix of elastic

constants becomes [41]:

$$\begin{pmatrix} C_{11} & C_{12} & C_{12} & 0 & 0 & 0 \\ C_{12} & C_{11} & C_{12} & 0 & 0 & 0 \\ C_{12} & C_{12} & C_{11} & 0 & 0 & 0 \\ 0 & 0 & 0 & C_{44} & 0 & 0 \\ 0 & 0 & 0 & 0 & C_{44} & 0 \\ 0 & 0 & 0 & 0 & 0 & C_{44} \end{pmatrix}. \quad (2.6)$$

To solve the equation of motion, (2.5), plane wave solutions of the form

$$u_i = u_{oi} e^{i(\vec{q}\cdot\vec{r} - \omega t)} \quad (2.7)$$

are assumed where u_{oi} is the amplitude. Substituting (2.7) into equation (2.5) and performing the necessary differentiations yields the secular equation

$$[\Gamma_{il} - \rho V^2 \delta_{il}] u_l = 0, \quad (2.8)$$

where $\Gamma_{il} = C_{ijkl} q_j q_k$, δ_{il} is the Kronecker delta and V is given by equation (2.2) for long wavelength acoustic waves. For nontrivial solutions it is necessary that

$$|\Gamma_{il} - \rho V^2 \delta_{il}| = 0, \quad (2.9)$$

where for cubic crystals,

$$\Gamma_{il} = \begin{cases} (C_{11} - C_{44})q_i^2 + C_{44}q^2 & i = l \\ (C_{12} + C_{44})q_i q_l & i \neq l \end{cases}. \quad (2.10)$$

Explicitly, equation (2.9) then becomes,

$$\begin{vmatrix} (C_{11} - C_{44})q_1^2 + \lambda & (C_{12} + C_{44})q_1q_2 & (C_{12} + C_{44})q_1q_3 \\ (C_{12} + C_{44})q_2q_1 & (C_{11} - C_{44})q_2^2 + \lambda & (C_{12} + C_{44})q_2q_3 \\ (C_{12} + C_{44})q_3q_1 & (C_{12} + C_{44})q_3q_2 & (C_{11} - C_{44})q_3^2 + \lambda \end{vmatrix} = 0, \quad (2.11)$$

where $\lambda = C_{44}q^2 - \rho V^2$ and ρ is the density of the solid. The q_i are the direction cosines of acoustic wavevector \vec{q} .

This is a cubic equation in ρV^2 and has been solved analytically by Every [42] to yield,

$$\rho V_\mu^2 = \frac{1}{3}C_1 + \frac{2}{3}C_2(1 - aS)^{\frac{1}{2}} \cos(\Psi + \frac{2}{3}\pi j), \quad (2.12)$$

where,

$$\begin{aligned} C_1 &= C_{11} + 2C_{44}, \quad C_2 = C_{11} - C_{44}, \quad C_3 = \frac{K}{C_{11} - C_{44}} \\ K &= C_{11} - C_{12} - 2C_{44}, \quad S = q_1^2q_2^2 + q_2^2q_3^2 + q_3^2q_1^2, \quad Q = q_1^2q_2^2q_3^2 \\ \Psi &= \frac{1}{3} \arccos\left[\frac{1 - \frac{3}{2}aS + bQ}{(1 - aS)^{\frac{3}{2}}}\right], \quad a = 3C_3(2 - C_3), \quad b = \frac{27}{2}C_3^2(3 - 2C_3). \end{aligned} \quad (2.13)$$

The index $j = 0, 1, 2$ and corresponds to $\mu = L, T_1$ and T_2 , respectively.

In the $\langle 100 \rangle$, $\langle 110 \rangle$ and $\langle 111 \rangle$ directions equation (2.12) is considerably simplified and can easily be solved to give the following acoustic wave velocities in the high symmetry directions:

$\langle 100 \rangle$ direction

$$V_L = \left[\frac{C_{11}}{\rho} \right]^{\frac{1}{2}}, \quad V_{T_1, T_2} = \left[\frac{C_{44}}{\rho} \right]^{\frac{1}{2}} \quad (2.14)$$

$\langle 110 \rangle$ direction

$$V_L = \left[\frac{C_{11} + C_{12} + 2C_{44}}{2\rho} \right]^{\frac{1}{2}}, \quad V_{T_1} = \left[\frac{C_{44}}{\rho} \right]^{\frac{1}{2}}, \quad V_{T_2} = \left[\frac{C_{11} - C_{12}}{2\rho} \right]^{\frac{1}{2}} \quad (2.15)$$

$\langle 111 \rangle$ direction

$$V_L = \left[\frac{C_{11} + 2C_{12} + 4C_{44}}{3\rho} \right]^{\frac{1}{2}}, \quad V_{T_1, T_2} = \left[\frac{C_{11} - C_{12} + C_{44}}{3\rho} \right]^{\frac{1}{2}}. \quad (2.16)$$

Knowledge of the elastic constants therefore allows for calculation of the acoustic velocity ratios which can provide a measure of the extent of the rotation-translation coupling mechanism.

2.3 Elasto-optic Coefficients of Cubic Crystals

The coupling between the strain of a crystal, $e_{kl}(\vec{r}, t)$, and the dielectric tensor, $\epsilon_{ij}(\vec{r}, t)$, is known as the photoelastic effect and is described by the equation [41]

$$\frac{-\delta\epsilon_{ij}(\vec{r}, t)}{\epsilon_0^2} = \sum_{k,l} p_{ijkl} e_{kl}(\vec{r}, t), \quad (2.17)$$

where the p_{ijkl} are the elasto-optic (or Pockel's) coefficients and $\epsilon_o = n^2$.

For cubic crystals there are only three independent elasto-optic coefficients p_{11} , p_{12} and p_{44} . Hence, equation (2.17) simplifies to

$$\frac{-\delta t_{ij}(\vec{r}, t)}{\epsilon_o^2} = 2p_{44}e_{ij}(\vec{r}, t) + (p_{11} - p_{12} - 2p_{44})\delta_{ij}e_{ij}(\vec{r}, t) + p_{12}\delta_{ij}\sum_k e_{kk}(\vec{r}, t). \quad (2.18)$$

From this it follows that the ratio of intensities of two Brillouin components is [13],

$$\frac{I_T}{I_L} = \left[\frac{\omega_L(\vec{q})|\xi^T|^2}{\omega_T(\vec{q})|\xi^L|^2} \right]^2, \quad (2.19)$$

where ω_μ is the angular frequency of acoustic mode μ and $\vec{\xi}^\mu$ is given by

$$\vec{\xi}^\mu = \hat{q} \times [\hat{q} \times [p_{44}\{(\hat{q} \cdot \hat{E}_o)\hat{\pi}^\mu + (\hat{\pi}^\mu \cdot \hat{E}_o)\hat{q}\} + (p_{11} - p_{12} - 2p_{44})\sum_l (\hat{q})_l(\hat{E}_o)_l(\hat{\pi}^\mu)_l \hat{1}_l + p_{12}(\hat{\pi}^\mu \cdot \hat{q})\hat{E}_o]] \quad (2.20)$$

for cubic crystals. Here, \hat{q} and \hat{E}_o are unit vectors in the direction of \vec{q} and the incident light wave respectively and $\hat{\pi}^\mu$ is the unit polarization vector of mode μ . The quantities $(\hat{\pi}^\mu)_l$, $(\hat{E}_o)_l$ and $(\hat{q})_l$ are the l th components of unit vectors $\hat{\pi}$, \hat{E}_o and \hat{q} , respectively. $\hat{1}_l$ ($l = 1, 2, 3$) are unit vectors along the cube axes. The vector $\vec{\xi}^\mu$ specifies the polarization of the radiation scattered from acoustic mode μ .

Hence, the intensities of the Brillouin components yield information about the elasto-optic interaction through the elasto-optic coefficients.

2.4 Derived Quantities

Many physical quantities can be determined once the complete set of elastic constants is known for a particular solid. Two of the more important and easily calculated elastic properties are the anisotropy factor, A , and the adiabatic bulk modulus, B . Explicitly, in terms of the elastic constants, these quantities are given by [13]

$$A = \frac{2C_{44}}{C_{11} - C_{12}} \quad (2.21)$$

and

$$B = \frac{C_{11} + 2C_{12}}{3} \quad (2.22)$$

for cubic systems.

For an elastically isotropic solid, $A = 1$. Approximate elastic isotropy was observed in light scattering experiments on the orientationally disordered phases of $(CH_2CN)_2$ [19], cyclooctane and O_2 [10]. Here $A = 0.85$, 0.90 and 1.02 for each of these solids, respectively, near their triple points. This isotropy also results in the near equality of the acoustic velocity ratios in all high symmetry directions for these three solids, as can be seen from Table 1.1. Near perfect elastic isotropy, in fact, also turns out to be a significant feature of β - C_2F_6 (as discussed in Chapter 5). It should also be noted that a characteristic of orientationally disordered crystals is a small bulk modulus (typically ~ 30 kbar).

Chapter 3

Experimental

3.1 Experimental Setup

The experimental setup in the present work is the standard one used for Brillouin scattering experiments in this laboratory and has been described in detail elsewhere [43]. It is shown in Figure 3.1.

Incident radiation at 514.5 nm was provided by a single-mode Ar^+ laser (Spectra Physics). This light was directed along the x-axis of the lab reference frame and focused at the scattering center by lens L1 (focal length = 40 cm). A front surface mirror (M) served to reflect the incident beam along the z-axis and up into the cryostat (CR). As a result the incident polarization was in the x-direction.

The scattered light was collected at 90° by collimating lens L2 (focal length = 20 cm) and entered a triple-pass, piezoelectrically scanned Fabry-Perot interferometer (FP). The diameter of aperture A3 was set at 0.75 cm resulting in a collection angle of about 2° . The light transmitted by the interferometer was focused by lens L3 (focal length = 80 cm) onto pinhole A4 (diameter = $800 \mu\text{m}$) and subsequently focused onto the cathode of a water-cooled photomultiplier tube (ITT FW 130) by lens L4. The output from the photomultiplier was fed to a data acquisition and stabilization system (Burleigh DAS-1) via an amplifier discriminator (AD). Other components included a temperature control

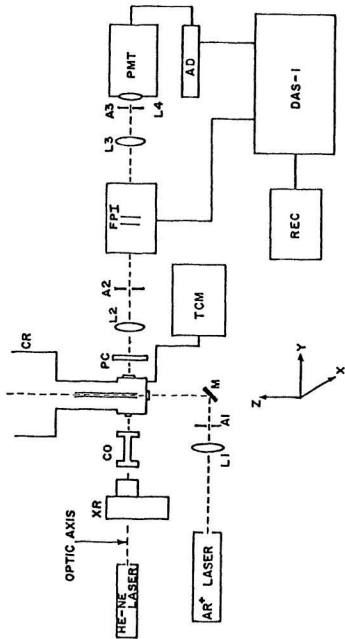


Figure 3.1: The complete experimental setup for Brillouin scattering experiments on $3-C_2F_6$.

unit (TCM), chart recorder (REC) and Laue X-ray diffraction apparatus (XR, CO and PC). These will be discussed in more detail in subsequent sections.

3.2 Cryostat

The single crystals of C_2F_6 used in these experiments were grown and maintained in a liquid nitrogen cryostat (Sulfrian Cryogenics Inc.) which was considerably modified for the present work. The modified tail section of this cryostat is shown in Figure 3.2.

The sample cell, which is housed in the cryostat, consists of a (3 mm *i.d.*, 5 mm *o.d.*) glass tube and is about 7 cm long. The lower end is sealed with a polished glass plug and sits in a springloaded BeCu jacket which is connected to a brass heat sink via two flexible copper braids. This assembly provides the necessary thermal contact to the cell while not restricting its rotation. At the top of the cell is a glass-to-kovar graded seal which allows the cell to be connected to a brass plate with low-melting-point solder. Crystals of cylindrical shape with diameter 3 mm and height 1 – 2 cm were grown in this cell. Cell rotation was achieved by turning a rotary-sealed knurled knob which was connected to the cell by two rigid stainless steel tubes and a brass plate. One of the stainless steel tubes was used for gas entry as can be seen in Figure 3.2.

Laser light entered the bottom of the cryostat along the z-axis of the lab frame through a fused quartz window and was scattered in all directions by the sample. Only light scattered at 90° in the y-direction was collected through a large plexiglass window.

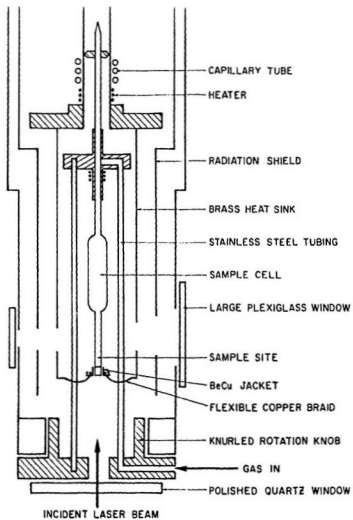


Figure 3.2: The cryostat tail section.

A smaller plexiglass window allowed X-rays to enter the cryostat and thus be diffracted by the sample through the large plexiglass window. Plexiglass was chosen for these windows because it is very transparent to X-rays.

Cooling to temperatures in the vicinity of the triple point of C_2F_6 was accomplished by allowing nitrogen from the inner reservoir, located in the main body of the cryostat, to flow through a thin capillary tube which was thermally linked to the bottom of the sample cell via the brass heat sink and copper braid/BeCu jacket assembly mentioned above. The flow of nitrogen through this tube was controlled by a fine needle valve at the top of the cryostat.

To partially compensate for the cooling and to control the temperature, three resistance wire heaters were strategically placed in close proximity to the cell. The first, with a resistance of 52 Ω , was located directly beneath the capillary tube and allowed for the 'smoothing out' of temperature fluctuations before they reached the sample. The second heater ($R = 36 \Omega$) was epoxied very near the bottom of the cell and permitted fine adjustment of the sample temperature. A third heater with resistance 51 Ω was placed near the top of the cell and could be used for controlling the temperature gradient between the top and bottom of the cell.

3.3 Temperature Sensing and Control

To monitor the temperature near the top and bottom of the cell, two GaAs diodes with a constant-current (10 μA) supply were used. The diodes were calibrated using the

triple point of C_2F_6 and a point at room temperature (determined from a mercury thermometer). A linear dependence of voltage on temperature was assumed. The topmost diode and heater were used in conjunction with a proportional feedback temperature controller. This device measured the voltage across the diode and compared it with a set-point voltage. If the diode voltage was higher than the set-point voltage (indicating a temperature slightly lower than desired) the controller would supply current to the heater to warm the area until the diode voltage equalled the set-point voltage. It should be noted here that initially the required temperature was reached approximately by controlling the flow of liquid nitrogen through the capillary tube with the needle valve (see previous section). Only after this was done could the heater provide enough heat to maintain the temperature without being saturated constantly due to excessive cooling from the nitrogen. Using this system, the temperature could be controlled to about ± 0.5 K.

A similar diode-heater-controller circuit was initially used at the bottom of the cell. It was, however, found that the resulting small-amplitude oscillations in temperature close to the nucleation site of the solid invariably resulted in a polycrystalline sample. Thus the heater and controller were disconnected and the diode voltage was monitored to determine the sample temperature.

3.4 Gas Handling System

Initially, the entire gas handling system was leak tested with a sensitive helium leak detector. Periodically (between runs) it was evacuated to a pressure of a few microns with a mechanical vacuum pump and left for a period of several days after which the

pressure was again checked to ensure that no leaks existed in the system. Once it was determined that the system was leak-tight, it was flushed four times with high purity gaseous hexafluoroethane to remove as much dust and foreign particles as possible. Following this thorough flushing procedure, the sample gas was admitted into the cell until a pressure of about 730 Torr was attained as indicated on the pressure gauge.

3.5 Growth of Crystals

Four large crystals were grown in the above system by admitting 99.6% pure gaseous C_2F_6 (Matheson) into the cell where it was cooled until it condensed. The sample temperature was then stabilized to about 1 K above and then abruptly lowered below the triple point. This resulted in a solid 2–3 mm in height which was usually left for several hours to anneal. The quality of this 'seed' was determined by using Laue X-ray diffraction (as discussed below). If the seed was polycrystalline it was melted and the growth procedure repeated. If it was a single crystal, it was grown to a height of 1 cm by slow cooling at a rate of about 0.1 K/h. Laue photographs were taken at various times during the cooling process. It was noted that as the crystal was grown it invariably became 'twinned'. This was probably due to a combination of a large temperature gradient and the crystal sticking to the walls of the cell. To minimize the adhering of the crystal to the cell walls, a small constant current was passed through the heater located on the BeCu jacket at the bottom of the cell. This warmed the walls of the cell prior to nucleation of the sample and seemed to help somewhat since the quality of crystals grown in this manner was slightly better. The diffraction spots, in all crystals kept for the light scattering experiments, remained fairly sharp and elliptical indicating little internal strain. Orientations with respect to the lab frame could be obtained using the standard

technique (see next section). A Laue diffraction picture of crystal #3 is shown in Figure 3.3.

3.6 Crystal Orientation and X-ray Apparatus

The X-rays necessary for the method of Laue (transmission) photography were provided by a Philips (MH101) X-ray source operated at 80 *kV*. The pictures were taken with a Polaroid (XR-7) Land camera located 10.7 *cm* away from the scattering center. A lead collimator reduced divergence of the beam before it reached the sample. Initial alignment of the collimator along the optic axis, defined by a He-Ne laser beam, ensured that the X-rays probed the scattering volume. To make certain that the incident X-ray beam was perpendicular to the plane of the film, the back reflection of the He-Ne beam, produced by a mirror temporarily fixed to the camera holder was made to coincide with the incident beam by adjustment of the holder. Once set to the proper position, it was left for the remainder of the experiments.

The crystal orientation with respect to the laboratory frame of reference (*xyz* shown in Figure 3.1) was defined in terms of the usual Euler angles (θ , ϕ , χ). To determine these angles Laue X-ray diffraction photographs were taken as the crystal was rotated through intervals of 7.5° as measured from a graduated scale fixed on the cryostat. It should be noted that the change in rotation angle of the cryostat corresponded to a change in Euler angle ϕ only. Using the center of the undiffracted X-ray beam as the origin, the *x-z* coordinates of all the diffraction spots on each picture were measured with a finely ruled rectangular grid to an accuracy much better than ± 1 *mm*. These coordinates, along with the crystal-film distance, then served as input data for a computer program

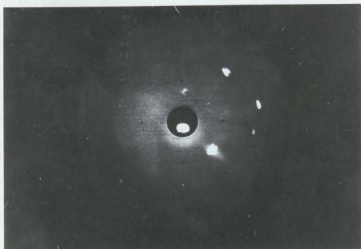


Figure 3.3: Laue diffraction photograph of crystal #3.

which utilized the method of stereographic projection to calculate possible sets of Euler angles for each photograph. The actual crystal orientation was found by comparing sets of Euler angles for various pictures until two sets were found in which θ and χ remained constant (within a degree or two due to slight cell wobble) and the difference in angle ϕ between the two equalled the corresponding change in cryostat angle. As a final check, a least squares crystal orientation program was run on each picture with the coordinates of the spots and the chosen Euler angles as input. The quality of the fit was examined and only orientations which gave an average error in measured and calculated coordinate distances of $< 1 \text{ mm}$ for all pictures were considered acceptable.

3.7 Laser

A Spectra-Physics Model 2020 argon ion laser served as the light source for these experiments. A prism in the laser cavity allowed selection of the 514.5 nm line in the Ar^+ spectrum while an intracavity Fabry-Perot etalon selected a single axial mode of this line. The resultant linewidth was of the order of $10 - 15 \text{ MHz}$ and was due mainly to frequency jitter. To maximize mechanical stability the laser was set on a floating granite block which rested upon a steel table.

3.8 Fabry-Perot Interferometer

The scattered light was analyzed with a piezoelectrically scanned triple-pass Fabry-Perot interferometer. This instrument consisted of two highly reflective parallel mirrors separated by a distance d . The rear mirror of the interferometer was mounted on three piezoelectric elements which facilitated continuous scanning of the plate separation. The

front mirror could be adjusted manually with three fine micrometer screws.

The frequency of the light, ν , passed by the Fabry-Perot for a given plate separation is determined by the resonance condition

$$2d = \frac{mc}{\nu}. \quad (3.1)$$

The frequency difference between two consecutive orders of interference is also determined by the plate separation and is known as the free spectral range of the interferometer. Mathematically, it is given by

$$FSR = \frac{c}{2d}. \quad (3.2)$$

The free spectral range for the present experiments was 10.99 GHz . This value was determined using a precision quartz sample for which the longitudinal and transverse Brillouin frequency shifts were well known [44], [45].

Another important characteristic of the Fabry-Perot interferometer is the finesse, \mathcal{F} , which is defined by

$$\mathcal{F} = \frac{FSR}{FWHM}, \quad (3.3)$$

where $FWHM$ is the full width at half-maximum of the intensity maximum. High finesse values were critical in these experiments as closely spaced spectral lines had to be resolved. With optimum alignment of all optical components and the interferometer

switched to triple pass, finesse values between 50 and 60 were obtained.

The triple pass option of the Fabry-Perot also caused the contrast (i.e. the ratio of maximum to minimum transmission intensity) to be cubed. The resulting rejection ratio of $\sim 1 : 10^6$ or more allowed very weak signals to be detected. The transverse Brillouin components were very weak in most spectra of $\beta\text{-C}_2\text{F}_6$ and hence triple passing of the scattered light by the interferometer was necessary to observe them.

3.9 Data Acquisition and Stabilization System

The data acquisition and stabilization system performed several important functions. The most important of these are listed below.

(i) The DAS employed a 1024 channel multichannel analyzer for accumulation and recording of spectra. The counts and corresponding channels were displayed on a CRT screen and a cursor was used to address a particular channel.

(ii) It provided the ramp voltage necessary for piezoelectric scanning of the interferometer. This ramp resembles a staircase where each step corresponds to incrementing the channel address scalar of the multichannel analyzer by one. The plate separation is a linear function of ramp voltage and hence each channel of the multichannel analyzer corresponds to a particular frequency passed by the Fabry-Perot interferometer.

(iii) Frequency drift caused by change in laser cavity length or interferometer plate separation due to temperature changes was automatically compensated for by the DAS. This was accomplished by locating a data window symmetrically about a preselected reference channel. A strong spectral feature (usually the Rayleigh line) was locked to this channel.

The counts on either side of this reference channel and within the window were stored in two registers. Following each sweep of the ramp the number of counts in the registers were compared. If they were unequal, indicative of frequency drift, a small correction voltage was automatically applied to the ramp scalar to bring the peak back towards the reference channel.

(iv) The DAS continuously optimized the interferometer finesse. A data window was again located symmetrically about the reference channel within the drift stabilization window. The counts in this window were stored in a register and maximized during a four sweep cycle. During sweep one the counts were accumulated and stored in the register. In sweep two of the ramp a test voltage was applied to the piezoelectric elements which tilted the rear mirror of the Fabry-Perot about a vertical axis. At the end of sweep two, the number of counts accumulated during sweeps one and two was compared and a correction voltage was applied to increase the number of counts. The second half of the procedure, involving sweeps three and four, was the same as the first half except the mirror was tilted about a horizontal axis.

(v) Another important feature of the DAS was the segmented time base. This allowed more time to be spent in specified regions of the spectrum and was used in the present work to obtain sufficient intensity of the Rayleigh component for drift stabilization and for more accurate determination of the frequency shifts of the transverse Brillouin components.

3.10 Optical System Alignment

Prior to accumulation of spectra, all components of the optical system were carefully aligned to ensure maximum transmission of the light scattered by the crystal. The first

step in this process was the removal of all lenses and the Fabry-Perot interferometer leaving only two pinholes - A4 near the photomultiplier and A3 near the location of the crystal as shown in Figure 3.1. A He-Ne laser beam was made to pass through both these pinholes and consequently defined the optic axis. The interferometer was then put in place between these two pinholes and its position adjusted until its back reflection coincided with the incident beam to ensure normal incidence. To obtain precise alignment of the Fabry-Perot the beam from the argon laser was scattered from a white card into the interferometer. A collimating lens was then placed in front of the interferometer and moved along the optic axis until parallel light was obtained. The front mirror of the Fabry-Perot was manually adjusted until a collapsing circular fringe pattern was observed. Good manual alignment at this stage was indicated by a single flashing spot produced by the Fabry-Perot as it was scanned repeatedly. A second lens was then inserted behind the Fabry-Perot and focused the analyzed light onto pinhole A4 and subsequently onto the cathode of the photomultiplier tube. Further fine adjustments of the interferometer mirrors, using the DAS-1 piezoelectric bias controls, were accomplished by maximizing the signal on the DAS-1 CRT screen. The corner cubes (retroreflectors) of the Fabry-Perot were then rotated to the triple pass position and final adjustments were made to maximize the signal.

3.11 Brillouin Spectra

The Brillouin spectra were collected over periods ranging from about 2 to 48 hours with a laser power of 50 mW and a free spectral range of 10.99 GHz.

To obtain as strong a spectrum as possible the incident laser beam was carefully

centered on the bottom of the cell as determined by observation of a back reflection of the beam. The Fabry-Perot interferometer was adjusted such that the Rayleigh peak was again maximized using the finesse optimization module of the DAS-1. This generally resulted in a finesse of 50-60.

With the Rayleigh peaks clearly visible in triple pass mode it was possible to maximize the intensity of the longitudinal Brillouin component. This was done by adjusting the front collecting lens (L2 in Figure 3.1) while observing the intensity of the longitudinal component on the DAS screen, using the segmented ramp feature, as the interferometer was repeatedly scanned. When the longitudinal component was maximized it was generally possible to see it in one 1 s scan of the interferometer.

When all conditions were optimized the central Rayleigh peak was locked by the DAS and accumulation of the spectrum began. Some of the spectra, once collected, were recorded using a chart recorder. The shifts and intensities of the Brillouin components of most spectra, however, were simply noted and no hard copy was obtained.

The channel numbers and intensities for peaks R , L , T_1 and T_2 were measured directly from the screen of the data acquisition system. The frequency shifts were then calculated according to the following:

$$\nu_L = \frac{FSR}{4} \sum_{i=1}^4 \frac{l_i}{r_i} \quad (3.4)$$

$$\nu_{T_1} = \frac{FSR}{4} \sum_{i=1}^4 \frac{s_i}{r_i} \quad (3.5)$$

$$\nu_{T_2} = \frac{FSR}{4} \sum_{i=1}^4 \frac{f_i}{r_i} \quad (3.6)$$

where FSR is the free spectral range and the remaining quantities are shown in Figure 3.4 [46]. This process of averaging minimized the effect of a slight scanning nonlinearity in the interferometer.

It was noticed, early in the experiments, that the Brillouin spectrum of $\beta\text{-C}_{20}$ exhibited a strong background. It was thought that this may have been obscuring the second transverse Brillouin component as only one had been observed up to this point. To eliminate some of this background a filter (of 10 nm bandwidth) was placed between the sample and the detection optics. No second transverse component was observed although the background was cut down significantly.

An attempt was also made to locate the second transverse Brillouin component by using the segmented time base feature of the DAS. Using the segmented ramp around the first transverse component on several occasions yielded two nearly degenerate peaks (a small dip in intensity was evident). These two peaks were taken to be the transverse Brillouin components in the nine spectra in which they were observed.

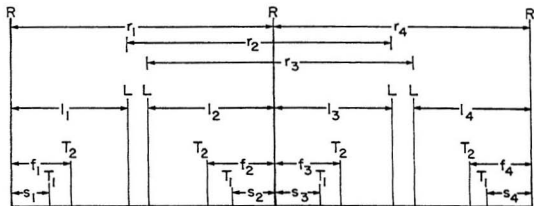


Figure 3.4: A Brillouin stick spectrum showing the Rayleigh peaks (R) and the various Brillouin components (T_1 , T_2 and L).

Chapter 4

Results

4.1 Brillouin Shifts and Intensities

In total, 60 Brillouin spectra were recorded for four independent crystals of $\beta\text{-CaF}_2$ at 169, 160 and 144 K. (It should be noted, from Table 4.1, that crystals 1, 3 and 4 have similar orientations. Clearly there was a preferred orientation for growth although the reason for this is unknown). Most spectra were obtained at 7.5° intervals of rotation in the angle ϕ . In all spectra the longitudinal Brillouin component (L) was clearly visible but the transverse Brillouin components (T_1 and T_2) were very weak and in all but 9 of the spectra only one was observed. A typical spectrum collected from crystal #1 at 169 K for a time of 26 hours, is shown in Figure 4.1. Here, the count rates are 2 and 35 counts/s for the transverse (T_1) and longitudinal (L) Brillouin components, respectively.

The observed Brillouin frequency shifts are shown in Tables 4.1, 4.2 and 4.3. As can be seen, the Brillouin shifts for the crystal orientations studied here were nearly identical and correspond to maximum variations of only 1% and 3% for the longitudinal and transverse shifts, respectively. These variations were not greatly different from the measurement uncertainty which is estimated to be about 1-2 channels (corresponding to about 0.05 GHz).

The ratios of transverse Brillouin component intensities to longitudinal Brillouin

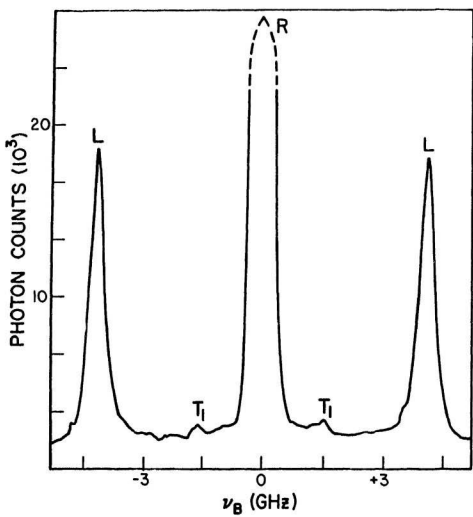


Figure 4.1: A typical Brillouin spectrum of $\beta\text{-C}_2\text{F}_6$.

component intensities, I_{T_1}/I_L and I_{T_2}/I_L , are also shown in Tables 4.1, 4.2 and 4.3 and are unusually small, varying from 0.01 to a maximum of only 0.10. These intensity ratios are probably accurate only to $\pm 15\%$ due to large variations in background intensity with channel number and weak signals.

Table 4.1: Brillouin scattering data for β - $C_{2}F_{6}$ at 169 K.

XL #	EULER ANGLES ($^{\circ}$)			OBSERVED (GHz)			CALCULATED (GHz)			OBSERVED		CALCULATED	
	θ	ϕ	χ	ν_L	ν_{T_1}	ν_{T_2}	ν_L	ν_{T_1}	ν_{T_2}	I_{T_1}/I_L	I_{T_2}/I_L	I_{T_1}/I_L	I_{T_2}/I_L
1	141.9	231.3	316.4	4.19	-	1.61	4.16	1.64	1.59	-	0.05	0.02	0.03
	141.7	228.7	316.6	4.20	-	1.64	4.17	1.64	1.58	-	0.08	0.02	0.01
	141.4	246.1	316.8	4.20	-	1.60	4.17	1.64	1.57	-	0.03	0.02	0.03
	141.2	253.5	316.9	4.20	-	1.63	4.17	1.64	1.56	-	0.04	0.02	0.02
	141.2	261.0	316.9	4.19	1.68	-	4.17	1.65	1.56	0.02	-	0.02	0.02
	142.2	268.7	317.1	4.18	1.62	-	4.17	1.65	1.57	0.04	-	0.03	0.01
	142.2	276.2	317.1	4.16	1.71	-	4.16	1.66	1.58	0.02	-	0.03	0.01
	141.7	283.7	317.1	4.15	1.59	-	4.15	1.67	1.59	0.04	-	0.03	0.01
	141.6	290.9	317.1	4.12	1.63	-	4.14	1.67	1.61	0.06	-	0.03	0.01
	141.6	298.2	317.2	4.11	1.67	-	4.14	1.67	1.62	0.05	-	0.02	0.01
	141.4	305.6	317.2	4.11	1.67	-	4.14	1.67	1.63	0.05	-	0.02	0.01
	141.3	312.9	317.2	4.12	1.66	-	4.14	1.66	1.64	0.04	-	0.02	0.00
	141.6	320.6	318.1	4.12	-	1.62	4.14	1.66	1.64	-	0.06	0.01	0.03
2	93.3	263.7	183.2	4.16	1.67	-	4.17	1.67	1.56	0.03	-	0.04	0.00
	94.6	271.2	183.4	4.14	1.69	-	4.16	1.67	1.55	0.04	-	0.04	0.00
	94.0	278.2	183.6	4.14	1.68	-	4.16	1.67	1.55	0.04	-	0.04	0.00
	94.0	285.7	183.5	4.15	1.70	-	4.17	1.66	1.56	0.03	-	0.05	0.00
	93.4	293.2	183.4	4.15	1.68	-	4.17	1.65	1.56	0.05	-	0.06	0.00
	93.0	301.5	183.4	4.17	1.67	-	4.17	1.64	1.57	0.06	-	0.07	0.02
	92.3	308.6	183.0	4.17	1.59	-	4.18	1.62	1.58	0.10	-	0.06	0.03
	92.5	316.0	183.2	4.17	1.60	-	4.18	1.61	1.58	0.06	-	0.05	0.05
	92.6	323.4	183.4	4.17	1.58	-	4.18	1.62	1.58	0.06	-	0.05	0.04
	92.8	337.8	184.1	4.16	1.65	-	4.17	1.64	1.57	0.08	-	0.07	0.01
	3	141.9	185.7	309.4	4.15	1.73	1.63	4.12	1.67	1.66	0.03	0.03	0.03
141.8		193.7	310.3	4.15	1.68	1.53	4.13	1.67	1.66	0.04	0.03	0.02	0.02
142.1		216.3	310.0	4.14	-	1.67	4.15	1.65	1.62	-	0.07	0.02	0.02
142.2		238.2	310.1	4.15	-	1.54	4.17	1.65	1.57	-	0.05	0.02	0.04
141.3		245.4	310.8	4.16	-	-	4.17	1.65	1.56	-	-	0.02	0.03
141.4		253.4	310.7	4.18	-	-	4.17	1.65	1.56	-	-	0.02	0.02
142.4		260.4	310.3	4.17	1.63	1.50	4.17	1.66	1.56	0.06	0.03	0.03	0.01
142.4		267.9	310.3	4.18	1.71	1.56	4.16	1.66	1.57	0.02	0.03	0.03	0.01
142.4	275.4	310.3	4.25	1.70	1.60	4.16	1.67	1.58	0.03	0.02	0.03	0.02	
142.4	282.0	310.3	4.18	1.69	1.60	4.15	1.67	1.59	0.03	0.03	0.02	0.02	
4	56.9	213.8	317.4	4.14	-	1.63	4.14	1.67	1.62	-	0.03	0.01	0.03
	57.2	221.0	317.5	4.10	1.67	1.61	4.13	1.67	1.64	0.03	0.03	0.01	0.03
	56.3	205.7	318.4	4.11	1.68	1.60	4.14	1.67	1.62	0.03	0.03	0.01	0.03
	57.2	281.2	317.5	4.16	-	1.55	4.16	1.66	1.58	-	0.02	0.01	0.04
	57.2	296.3	317.5	4.16	-	-	4.17	1.66	1.56	-	-	0.01	0.02

Table 4.2: Brillouin scattering data for β - C_2F_6 at 160 K.

Xl.	EULER ANGLES ($^\circ$)			OBSERVED (GHz)			CALCULATED (GHz)			OBSERVED		CALCULATED	
	#	β	ϕ	χ	ν_L	ν_T	ν_T	ν_L	ν_T	ν_T	Γ_T/Γ_L	Γ_T/Γ_L	Γ_T/Γ_L
1	141.9	231.3	316.4	4.34	-	1.67	4.34	1.67	1.64	-	-	0.01	0.02
	141.4	246.1	316.8	4.32	-	1.63	4.34	1.67	1.63	-	0.07	0.01	0.02
	141.2	261.0	316.9	4.36	1.60	-	4.34	1.67	1.63	0.01	-	0.01	0.01
	142.2	276.2	317.1	4.34	1.69	-	4.33	1.68	1.64	0.01	-	0.02	0.01
	141.7	283.7	317.1	4.33	1.68	-	4.33	1.68	1.64	0.03	-	0.02	0.01
	141.6	298.2	317.2	4.32	1.68	-	4.32	1.68	1.66	0.04	-	0.02	0.01
	141.3	312.9	317.2	4.34	1.68	-	4.32	1.68	1.67	0.06	-	0.01	0.01
	141.6	320.6	318.1	4.31	-	1.67	4.32	1.68	1.67	-	0.07	0.01	0.02
2	94.0	285.7	183.5	4.34	1.70	-	4.34	1.68	1.62	0.05	-	0.03	0.00
	93.4	293.2	183.4	4.34	1.68	-	4.34	1.67	1.63	0.06	-	0.04	0.00
	93.0	301.5	183.4	4.34	1.66	-	4.34	1.67	1.63	0.05	-	0.04	0.01
	92.3	308.6	183.0	4.33	1.64	-	4.34	1.66	1.63	0.06	-	0.04	0.02
	92.5	316.0	183.2	4.33	1.66	-	4.34	1.65	1.64	0.06	-	0.03	0.03
	92.6	323.4	183.4	4.34	1.64	-	4.34	1.65	1.64	0.06	-	0.04	0.02
	92.1	330.9	182.8	4.34	1.66	-	4.34	1.66	1.63	0.05	-	0.04	0.01
	92.8	337.8	184.1	4.35	1.65	-	4.34	1.67	1.63	0.05	-	0.05	0.01

Table 4.3: Brillouin scattering data for β - C_2F_6 at 144 K.

Xl.	EULER ANGLES ($^\circ$)			OBSERVED (GHz)			CALCULATED (GHz)			OBSERVED		CALCULATED	
	#	β	ϕ	χ	ν_L	ν_T	ν_T	ν_L	ν_T	ν_T	Γ_T/Γ_L	Γ_T/Γ_L	Γ_T/Γ_L
1	141.9	231.3	316.4	4.63	-	1.68	4.63	1.73	1.68	-	0.07	0.01	0.03
	141.4	246.1	316.8	4.64	-	1.74	4.62	1.75	1.68	-	0.02	0.01	0.03
4	57.5	236.0	317.4	4.64	-	1.64	4.67	1.65	1.64	-	0.03	0.03	0.01
	57.5	251.6	317.4	4.67	1.67	1.58	4.67	1.66	1.64	0.02	0.02	0.02	0.02
	56.3	265.7	318.4	4.67	1.67	-	4.66	1.70	1.64	0.02	-	0.01	0.01
	57.2	296.3	317.5	4.64	-	-	4.63	1.76	1.65	-	-	0.01	0.01

4.2 Elastic Constants

In addition to the Brillouin frequency shift data, a knowledge of the density and refractive index of solid C_2F_6 was required to determine the elastic constants. For C_2F_6 only one value for the density of the solid could be found in the literature. This is $\rho = 1.85 \text{ g/cm}^3$ at the melting point (172.6 K) [47]. The lattice parameter for the orientationally disordered phase, however, has been determined by neutron diffraction experiments at 95 and 110 K [28]. Since there is some uncertainty as to whether a phase transition occurs at

104 K only the 110 K value of lattice parameter, $a = 6.1412 \text{ \AA}$, was used for calculation of the density at this temperature. Using a molar mass of $M = 138.012 \text{ g/mol}$ [48] a density of 1.98 g/cm^3 was determined using this lattice parameter. The temperatures of interest in this work lie between 172.6 K and 110 K and thus linear interpolation was used to obtain the necessary densities. Because these density values were determined from two completely different sources, the assumed dependence of density on temperature for C_2F_6 was compared with that of SF_6 [7]. The slopes were nearly identical ($-2.07 \times 10^{-3} \text{ g/cm}^3\text{K}$ for C_2F_6 and $-2.06 \times 10^{-3} \text{ g/cm}^3\text{K}$ for SF_6) which suggests that the densities of C_2F_6 used here are probably reliable. The densities calculated using this method are given in Table 4.4.

No values of the refractive index of solid C_2F_6 could be found in the literature. A value of $n_l = 1.206$ at 199.9 K for the liquid [48], however, was available. The density at this temperature was calculated from an empirical expression determined by Ruff and Bretschneider [47]. This expression, although old, gave liquid densities which were practically identical (better than 0.5%) to current accepted densities at various temperatures [48], [49]. The Lorentz-Lorenz relation,

$$\frac{n_s^2 - 1}{n_s^2 + 2} = \frac{\rho_s (n_l^2 - 1)}{\rho_l (n_l^2 + 2)}, \quad (4.1)$$

was then used to determine the refractive indices at the desired temperatures. Here, ρ is the density, n is the refractive index, and the subscripts s and l denote the solid and liquid, respectively. The values obtained for the refractive index are given in Table 4.4. It should be noted that these values are in good agreement (better than 1%) with values

Table 4.4: Temperature dependent data for β - C_2F_6 .

TEMPERATURE (K)	DENSITY (g/cm^3)	REFRACTIVE INDEX	C_{11} (kbar)	C_{12} (kbar)	C_{44} (kbar)
169	1.857	1.243	26.99 ± 0.10	19.32 ± 0.10	4.44 ± 0.04
160	1.876	1.246	29.76 ± 0.07	21.34 ± 0.05	4.53 ± 0.02
144	1.909	1.251	35.32 ± 0.20	25.21 ± 0.41	4.33 ± 0.09

of refractive index obtained from the experimental molar polarizability for C_2F_6 [50].

The elastic constants, for each temperature, were determined using a computerized iterative least squares fit procedure [51]. The necessary input included the density, refractive index, Euler angles, and measured Brillouin shifts as well as initial guesses of the elastic constants. For each cycle of iteration, the acoustic wave velocities, V_μ were calculated from equation (2.11) for each crystal orientation. The frequencies $\nu(C_{ij})$ were then determined from the Brillouin equation (2.4). The differences between the observed and calculated frequencies were minimized by a least squares fit procedure based on Newton's method. The term which was minimized with respect to variation of the elastic constants was

$$\chi^2(C_{ij}) = \frac{1}{N-3} \sum_{k=1}^N \left(\frac{\nu_k^{CALC}(C_{ij}) - \nu_k^{OBS}}{\sigma_k} \right)^2, \quad (4.2)$$

where N is the total number of frequency shifts and σ_k is a weighting factor representing the estimated standard deviation of the k th frequency shift measurement. For this work σ_k was varied from 0.01 to 0.04 GHz. This implied that σ_k equalled about one standard

deviation.

Initially it was impossible to determine whether the single transverse peak observed in most of the spectra was the slow or fast transverse Brillouin component. Thus a complete analysis was first carried out assuming that the component was the slow transverse and then repeated assuming it was the fast transverse. The elastic constants obtained in both cases agreed with each other to better than 0.5%. The final assignments (T_1 or T_2) of the single transverse components were determined using the intensity ratios, I_{T_1}/I_L and I_{T_2}/I_L , calculated with the iterative least squares elasto-optic coefficient computer program. The transverse component with the greater calculated intensity ratio was the assignment given to the observed peak.

The best-fit elastic constants, given in Table 4.4, were those which minimized χ^2 . The uncertainties quoted in Table 4.4 are those for which $\chi^2 = 1$ and are therefore the relative errors and express the quality of the least squares fit. In addition to the relative errors, an additional estimated systematic error of about 2% is present due to uncertainties in the density, refractive index and scattering angle. This systematic error does not affect the elastic constant ratios and hence also not the acoustic velocity ratios.

The temperature dependences of elastic constants C_{11} and C_{12} appear to be linear with slopes $\Delta C_{11}/\Delta T = -0.335 \pm 0.010$ and $\Delta C_{12}/\Delta T = -0.236 \pm 0.010$, whereas C_{44} appears to be independent of temperature with $\Delta C_{44}/\Delta T = 0.005 \pm 0.011$ kbar/K in the temperature range investigated here. The errors quoted are the standard errors only. A graph of the elastic constants as functions of temperature is shown in Figure 4.2.

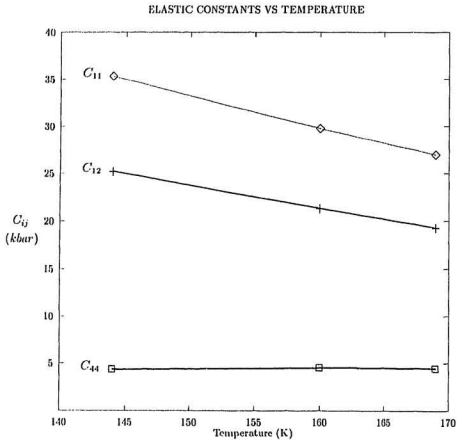


Figure 4.2: Adiabatic elastic constants of β - C_2F_6 as a function of temperature. The uncertainties are approximately the size of the symbols.

4.3 Elasto-optic Coefficients

The elasto-optic coefficient ratios were determined using an iterative least squares procedure analogous to that used for the elastic constants. Here, initial values of p_{12}/p_{11} and p_{44}/p_{11} were varied until a reasonable agreement between the calculated and observed intensity ratios, I_{T_1}/I_L and I_{T_2}/I_L , was achieved. Again the quality of the fit was determined by the value of χ^2 . As discussed above it was impossible to determine whether the single transverse component observed in most spectra was T_1 or T_2 . The assignments which resulted in the smallest χ^2 were taken to be the correct ones and are given in Tables 4.1, 4.2 and 4.3.

Estimated absolute values of the elasto-optic coefficients can be determined from the approximate expression [52],

$$p_{11} + 2p_{12} = \frac{(\epsilon - 1)(\epsilon + 2)}{\epsilon^2}, \quad (4.3)$$

where $\epsilon = n^2$. The elasto-optic coefficient ratios determined using the procedure outlined above as well as the absolute values calculated from equation (4.3) are given in Table 4.5.

Table 4.5: Elasto-optic ratios and coefficients for $\beta\text{-C}_2\text{F}_6$.

TEMPERATURE (K)	p_{12}/p_{11}	p_{44}/p_{11}	p_{11}	p_{12}	p_{44}
169	1.10	0.12	0.25	0.28	0.03
160	1.06	0.09	0.26	0.28	0.02
144	1.04	0.12	0.27	0.28	0.03

The uncertainties in the elasto-optic coefficient ratios are probably of the order of

10 – 20%. This is because it is the sum of the intensities, $I_{T_1} + I_{T_2}$, that was actually measured as the transverse components seem to be nearly degenerate.

4.4 Derived Quantities

The adiabatic bulk modulus, B , and the elastic anisotropy, A , were determined from the best-fit elastic constants using equations (2.21) and (2.22), at the temperatures investigated. The values obtained for these quantities are given in Table 4.6. B clearly increases with decreasing temperature whereas A decreases.

Table 4.6: Adiabatic bulk modulus and anisotropy factor for β - C_2F_6 .

TEMPERATURE (K)	B (kbar)	A
169	21.9 ± 0.1	1.16 ± 0.04
160	24.1 ± 0.1	1.08 ± 0.03
144	28.6 ± 0.4	0.86 ± 0.08

Chapter 5

Discussion

5.1 Results for C_2F_6

The Brillouin spectra and elastic constants of $\beta\text{-}C_2F_6$ provide a wealth of information about both its bulk and molecular properties. These features are discussed in the following paragraphs.

The Brillouin spectra of $\beta\text{-}C_2F_6$ are somewhat unusual in that the frequency shifts of the Brillouin components did not depend significantly on crystal orientation. Hence $\beta\text{-}C_2F_6$ is elastically quite isotropic with an elastic anisotropy, $A \sim 1$ for all temperatures investigated.

The Cauchy relation $C_{12}/C_{44} = 1$, for central intermolecular forces in cubic crystals, is not obeyed by $\beta\text{-}C_2F_6$. In fact, a high value of $C_{12}/C_{44} = 4.4$ is found at 169 K and suggests that angle-dependent forces play an important role in the dynamics of this orientationally disordered solid. This was expected because of the large degree of rotational freedom of the molecules on their lattice sites.

A quantitative estimate of the extent of the rotation-translation coupling in $\beta\text{-}C_2F_6$ can be obtained from the density independent ratios of acoustic velocities in high symmetry directions. Large values of these ratios indicate softened transverse mode(s) which,

as mentioned earlier, may be interpreted as being due to rotation-translation coupling [13].

In order to get an idea of the strength of the rotation-translation coupling in β - C_2F_6 these ratios have been calculated from the elastic constants determined in the present work and are given in Table 5.1, along with, for the purpose of comparison, those for the rare gas solids at temperatures near their respective triple points. As is evident, three of these ratios are substantially larger than the corresponding ratios for the rare gas solids and hence suggest that rotation-translation coupling is present in C_2F_6 . The near equality of all four ratios for β - C_2F_6 is a consequence of its near perfect elastic isotropy.

Table 5.1: Temperature dependence of ratios of acoustic velocities in high symmetry directions for β - C_2F_6 .

SOLID	$\langle 100 \rangle$	$\langle 111 \rangle$	$\langle 110 \rangle$	$\langle 110 \rangle$
	$V_L/V_{T_2, T_1}$	$V_L/V_{T_2, T_1}$	V_L/V_{T_2}	V_L/V_{T_1}
<i>Ne, Ar, Kr, Xe</i> [13]	1.44	2.24	1.65	2.71
$C_2F_6(169\text{ K})$	2.47	2.62	2.49	2.68
$C_2F_6(160\text{ K})$	2.56	2.64	2.58	2.67
$C_2F_6(144\text{ K})$	2.87	2.67	2.83	2.62

5.2 Comparison to other Orientationally Disordered Molecular Solids

As previously mentioned, preliminary molecular dynamics simulations of β - C_2F_6 [33], [34] indicate that strong rotation-translation coupling exists in the $q = 0$ wavevector regime. This is consistent with the values for the acoustic velocity ratios given in Table 5.1 in that three of these ratios are substantially larger than the corresponding ratios for

the rare gas solids and are therefore indicative of significantly softened transverse modes. This suggests that moderately strong rotation-translation coupling exists near $q = 0$. However, the molecular dynamics simulations calculations also suggest that C_2F_6 is very similar to SF_6 . This, from the present work, does not appear to be the case, as SF_6 behaves elastically like a rare gas solid. In addition, no evidence for rotation-translation coupling was observed near the Brillouin zone center for SF_6 [7].

The ratios in Table 5.2 suggest that β - C_2F_6 is elastically quite isotropic and thus seems to be qualitatively similar to cyclooctane and O_2 [10] although its acoustic velocity ratios are not quite as large. Brillouin scattering experiments [10] on cyclooctane and O_2 have shown that strong rotation-translation coupling exists in these solids. In cyclooctane this strong coupling was attributed to the fact that the molecular reorientation frequency (~ 1 GHz) is of the order of the transverse acoustic mode frequency (~ 2 GHz). A somewhat similar situation exists in O_2 where the frequencies of molecular vibrational dephasing are approximately 3 and 5 GHz [53] for the disklike and spherically rotating molecules respectively and are of the order of the acoustic wave frequencies.

Table 5.2: Ratios of acoustic velocities in high symmetry directions for several molecular solids near their triple points.

SOLID	$\langle 100 \rangle$	$\langle 111 \rangle$	$\langle 110 \rangle$	$\langle 110 \rangle$
	$V_L/V_{T_2,T_1}$	$V_L/V_{T_2,T_1}$	V_L/V_{T_2}	V_L/V_{T_1}
<i>Ne, Ar, Kr, Xe</i> [13]	1.44	2.24	1.65	2.71
SF_6 [7]	1.60	2.29	1.76	2.64
C_8H_{16} (cyclooctane) [10]	3.49	3.35	3.48	3.29
O_2 [10]	3.07	3.09	3.07	3.10
$(CH_2CN)_2$ [14]	2.79	2.60	2.76	2.54
C_2F_6	2.47	2.62	2.49	2.68

It was suggested [10] that the elastic isotropy exhibited by cyclooctane and O_2 was

due to an averaging out of the rotational motion of the disklike molecules on the unit cell faces. The isotropy was found to be greatest near the triple point for O_2 and decreased with decreasing temperature. This feature was consistent with the proposed rotation-translation coupling effect.

As can be seen in Table 5.2, the similarity between C_2F_6 and $(CH_2CN)_2$ is striking. Both are nearly elastically isotropic and the acoustic velocity ratios in the high symmetry directions for both solids are nearly equal. It is therefore relevant to consider related work on $(CH_2CN)_2$ as it may provide some insight into the elastic behaviour and the rotation-translation coupling mechanism in β - C_2F_6 .

$(CH_2CN)_2$ exists in an orientationally disordered phase from its triple point at 331 K to 233 K [19]. Dielectric studies [54] have suggested very little change in the nature of molecular reorientation between the liquid and orientationally disordered phase. Light scattering experiments on $(CH_2CN)_2$ [14] have been carried out for temperatures in the range 243 K to 323 K. A pair of peaks in the polarized spectra, thought to be due to transverse phonons, was observed above 283 K but did not appear below this temperature. The intensity of these peaks increased with increasing temperature and they could easily be seen at 323 K. It was suggested [14] that the temperature dependence of the shear phonon intensities is related to the temperature dependence of the reorientation mechanism. Therefore at low temperatures, when the molecular reorientational frequency is close to that of the transverse phonon frequency, the slowly reorienting molecules might dampen the shear phonons. At high temperatures these frequencies differ by about an order of magnitude and thus the coupling may be weaker. Rayleigh-Brillouin measurements of the depolarized light scattering in $(CH_2CN)_2$ [55]

have found shear wave peaks with resonance line shapes. These spectra were understood as arising from coupling between acoustic phonons and molecular reorientational motions and constitute evidence for rotation-translation coupling in $(CH_2CN)_2$. A hydrodynamic model developed by Courtens [5], which included coupling between molecular reorientation and acoustic modes, correctly predicted the features of the depolarized light scattering spectra as well as the ultrasonic values of the elastic constants. Further investigations by Descamps [56] indicate that steric hindrance is present in $(CH_2CN)_2$. It was later noted, by Press *et al.* [57], that in larger molecules, such as $(CH_2CN)_2$, steric hindrance introduces rotation-translation coupling.

More recent work on plastic $(CH_2CN)_2$ has revealed several other interesting points. Derollez *et al.* [58] deduced the rotation-translation coupling in the disordered phase of deuterated succinonitrile from X-ray diffraction measurements. It was shown that the coupling is directly related to the spatial siting of neighbouring molecules and that it affects the positions of the gauche isomers. In a later study by the same group [59], the structure of plastic $(CH_2CN)_2$ was re-examined through extended X-ray diffraction measurements. The structure was solved by using both the analytic procedures of symmetry-adapted functions and a Frenkel model assuming discrete orientations. A possible rotation-translation coupling was included in the latter case via an offset vector.

The nature of the rotational motions in $(CH_2CN)_2$ has been examined by various techniques including NMR [60], dielectric relaxation [61], Rayleigh scattering [62], incoherent neutron scattering [63], [64] and molecular dynamics simulation [65]. All of these have revealed dynamic orientational disorder of the molecules with the rotational disorder

being due to jumps from one cube diagonal to another and trans-gauche isomerization.

The fact that C_2F_6 is similar to $(CH_2CN)_2$ and very different from SF_6 is quite interesting since all three have the same site symmetry and the orientationally disordered phases form body-centered cubic lattices. All three, however, have different molecular symmetries. Molecular symmetry, therefore, probably does not play a significant role in the dynamics and, in particular, the rotation-translation coupling mechanism and its strength. If it did play an important role, C_2F_6 would be expected to behave very similarly to SF_6 because of their nearly identical molecular symmetries (as suggested by the molecular dynamics simulations of Dove and Lynden-Bell [33]). C_2F_6 , instead, was found to behave elastically like $(CH_2CN)_2$ which has a very different molecular symmetry (the gauche isomer has symmetry 2 and the trans isomer has symmetry $2/m$ [59]). For comparison, the elastic constants of these three orientationally disordered solids along with those of Xe are given in Table 5.3.

A possible explanation for the extreme difference of behaviour between C_2F_6 and SF_6 could be that the reorientational frequency of the molecules of C_2F_6 in the disordered phase is comparable to the frequency of the transverse acoustic phonons, whereas in SF_6 these two frequencies are quite different. It was suggested [7] that in SF_6 the molecular reorientational motion is effectively 'smeared out'. Thus stronger rotation-translation coupling would be expected in C_2F_6 than in SF_6 . This seems to be a plausible explanation since it appears that the slight difference in molecular symmetry of the two cannot account for such a difference, as discussed above.

A second factor which certainly accounts, at least in part, for the very different

behaviour of C_2F_6 and SF_6 , and which seems to have been overlooked in the molecular dynamics simulations calculations [33], [34], is the existence of internal rotational motion in β - C_2F_6 . In β - C_2F_6 , in addition to the molecular tumbling-like motions, there also exists rotation of one CF_3 group with respect to the other and overall rotation about the $C-C$ bond. This type of motion also occurs in C_2Cl_6 [31] and an analogous phenomenon takes place in $(CH_2CN)_2$ [58], [59] as the $CH_2-C \equiv N$ groups rotate about the central $C-C$ bond (in doing so, one isomer is changed into another). This type of motion does not occur in SF_6 . It will, however, certainly influence the rotation-translation coupling in β - C_2F_6 , especially if the frequency of these rotational motions is of the order of the frequency of the transverse acoustic phonons. The fact that C_2F_6 exhibits internal and molecular reorientational motions similar to those of $(CH_2CN)_2$ and quite distinct from those of SF_6 probably accounts for both the surprising similarities observed between C_2F_6 and $(CH_2CN)_2$ and the pronounced differences between C_2F_6 and SF_6 .

Table 5.3: Elastic constants of Xc , SF_6 , $(CH_2CN)_2$ and C_2F_6 near their triple points.

CRYSTAL	T (K)	C_{11}	C_{12}	C_{44}	C_{12}/C_{44}	B (kbar)	Λ
Xc [66]	156	29.8	19.0	14.8	1.28	22.6	2.74
SF_6 [7]	221.0	34.09	22.18	13.23	1.68	26.1	2.22
$(CH_2CN)_2$ [67]	323.2	45.8	32.4	6.5	4.98	36.9	0.97
C_2F_6	169	26.99	19.32	4.44	4.35	21.9	1.16

5.3 Conclusion

In summary, the elastic and elasto-optic constants of the orientationally disordered phase of C_2F_6 have been determined using the technique of high resolution Brillouin spectroscopy. The ratios of acoustic velocities calculated from the elastic constants show that C_2F_6 is quite isotropic and that it exhibits moderately strong rotation-translation

coupling and in these respects is very similar to $(CH_2CN)_2$. This is in contrast to SF_6 which behaves like a rare gas solid.

References

- [1] N.G. Parsonage and L.A.K. Staveley, *Disorder in Crystals* (Clarendon, Oxford, 1978).
- [2] *The Plastically Crystalline State*, J.N. Sherwood, Ed. (Wiley, New York, 1979).
- [3] S.M. Rytov, *Sov. Phys. JETP* **6**, 130, 401, 513 (1958).
- [4] R.M. Lynden-Bell, I.R. McDonald and M.L. Klein, *Mol. Phys.* **48**, 1093 (1983).
- [5] E. Courtens, *J. Phys. (Paris)* **37**, L-21 (1976).
- [6] V. Askarpour, Ph.D. Thesis, Memorial University of Newfoundland, 1991 (Unpublished).
- [7] H. Kiefte, R. Penney and M.J. Clouter, *J. Chem. Phys.* **88**, 5846 (1988).
- [8] J. Zuk, D.M. Brake, H. Kiefte and M.J. Clouter, *J. Chem. Phys.* **91**, 5285 (1989).
- [9] J. Zuk, H. Kiefte and M.J. Clouter, *J. Chem. Phys.* **92**, (1990).
- [10] H. Kiefte, V. Askarpour, J. Zuk and M.J. Clouter, *J. Phys. Chem.* **96**, 1449 (1992).
- [11] S.C. Rand and B.P. Stoicheff, *Can. J. Phys.* **60**, 287 (1982).
- [12] S. Wonneberger and A. Hüller, *Z. Phys.* **B66**, 191 (1987).
- [13] B.P. Stoicheff, in *Rare Gas Solids Volume II*, M.L. Klein and J.A. Venables Ed. (Academic, London, 1976).

- [14] M.J. Bird, D.A. Jackson and H.T.A. Pentecost, in *Proc. 2nd Int. Conf. on Light Scattering in Solids*, M. Balkanski, Ed. (Flammarion, Paris, 1971).
- [15] S.V. Marx and R.O. Simmons, *J. Chem. Phys.* **81**, 944 (1984).
- [16] M. More and R. Fourct, *Discuss. Faraday Soc.* **69**, 75 (1980).
- [17] M.T. Dove and R.M. Lynden-Bell, *J. Phys.* **C19**, 3343 (1986).
- [18] I.R. McDonald, D.G. Bounds and M.L. Klein, *Mol. Phys.* **45**, 521 (1982).
- [19] L. Boyer, R. Vacher, M. Adam and L. Cecchi, in *Proc. 2nd Int. Conf. on Light Scattering in Solids*, M. Balkanski, Ed. (Flammarion, Paris, 1971).
- [20] K.H. Michel and J. Naudts, *Phys. Rev. Lett.* **39**, 212 (1977).
- [21] K.H. Michel and J. Naudts, *J. Chem. Phys.* **67**, 547 (1977).
- [22] K.H. Michel and J. Naudts, *J. Chem. Phys.* **68**, 216 (1978).
- [23] J.M. Rowe, J.J. Rush, N. Vagelatos, D.L. Price, D.G. Hinks and S. Susman, *J. Chem. Phys.* **62**, 4551 (1975).
- [24] W. Krasser, U. Buchenau and S. Haussuhl, *Solid State Comm.* **18**, 287 (1976).
- [25] S. Haussuhl, *Solid State Comm.* **13**, 147 (1973).
- [26] C.H. Wang and S.K. Satija, *J. Chem. Phys.* **67**, 851 (1977).
- [27] E.L. Pace and J.G. Aston, *J. Am. Chem. Soc.* **70**, 566 (1948).
- [28] B.M. Powell, W.Press, G. Dolling and V.F. Sears, *Mol. Phys.* **53**, 941 (1984).
- [29] H.S. Gutowsky and G.E. Pake, *J. Chem. Phys.* **18**, 162 (1950).

- [30] A. Lewis and E.L. Pace, *J. Chem. Phys.* **58**, 3661 (1973).
- [31] T. Koide, M. Tsujino, K. Sawada and T. Oda, *Bull. Chem. Soc. Japan* **47**, 2998 (1974).
- [32] R.O. Simmons, Private communication.
- [33] M.T. Dove and R. Lynden-Bell, in *Dynamics of Molecular Crystals*, J. Lascombe, Ed. (Elsevier, Grenoble, 1986).
- [34] M.T. Dove, *Oriental Disorder in Crystals* **6**, 6 (1987).
- [35] M.T. Dove and G.S. Pawley, *J. Phys.* **C16**, 5969 (1983).
- [36] M.T. Dove and G.S. Pawley, *J. Phys.* **C17**, 6581 (1984).
- [37] M.T. Dove, G.S. Pawley, G. Dolling and B.M. Powell, *Mol. Phys.* **57**, 865 (1986).
- [38] G. Dolling, B.M. Powell and V.F. Sears, *Mol. Phys.* **37**, 1859 (1979).
- [39] G.B. Benedek and K. Fritsch, *Phys. Rev.* **149**, 647 (1966).
- [40] L.D. Landau and E.M. Lifshitz, *Theory of Elasticity* (Pergamon, Oxford, 1970).
- [41] J.F. Nye, *Physical Properties of Crystals* (Clarendon, Oxford, 1957).
- [42] A.G. Every, *Phys. Rev. Lett.* **42**, 1065 (1979).
- [43] S.F. Ahmad, H. Kieft, M.J. Clouter and M.D. Whitmore, *Phys. Rev.* **B20**, 4239 (1982).
- [44] G.E. Durand and A.S. Pine, *IEEE J. Quant. Electron.* **4**, 523 (1968).
- [45] J. Pelous and R. Vacher, *Solid State Comm.* **16**, 279 (1975).

- [46] S.C. Rand, Ph.D. Thesis, University of Toronto, 1978 (Unpublished).
- [47] V.O. Ruff and O. Bretschneider, *Z. Anorg. u. Allg. Chem.* **210**, 173 (1933).
- [48] W. Braker and A.L. Mossman, in *Matheson Gas Data Book* (Matheson, Secaucus).
- [49] N. Marshall, in *Gas Encyclopedia* (Elsevier, New York, 1976).
- [50] R. Bohmer and A. Loidl, *J. Chem. Phys.* **94**, 2143 (1991).
- [51] R.A. McLaren, Ph.D. Thesis, University of Toronto, 1973 (Unpublished).
- [52] D.W. Oxtoby and V. Chandrasekaran, *Phys. Rev.* **B16**, 1706 (1977).
- [53] H. Kieft, M.J. Clouter, N.H. Rich and S.F. Ahmad, *Chem. Phys. Lett.* **70**, 425 (1980).
- [54] D.E. Williams and C.P. Smyth, *J. Am. Chem. Soc.* **84**, 1808 (1962).
- [55] T. Bischofberger and E. Courtens, *Phys. Rev. Lett.* **35**, 1451 (1975).
- [56] M. Descamps, *Solid State Comm.* **14**, 77 (1974).
- [57] W. Press, H. Grimm and A. Hüller, *Acta Crystallogr.* **A35**, 881 (1979).
- [58] P. Derollez, J. Lefebvre, M. Descamps, W. Press and H. Grimm, *J. Phys.: Condens. Matter* **2**, 9975 (1990).
- [59] P. Derollez, J. Lefebvre, M. Descamps, W. Press and H. Fontaine, *J. Phys.: Condens. Matter* **2**, 6893 (1990).
- [60] J.G. Powles, A. Begum and M.O. Norris, *Mol. Phys.* **17**, 489 (1969).
- [61] W. Longueville, H. Fontaine and A. Chapoton, *J. Chim. Phys.* **68**, 436 (1971).

- [62] L. Boyer, R. Vacher, L. Cecchi, M. Adam and P. Berge, *Phys. Rev. Lett.* **26**, 1435 (1971).
- [63] R.E. Lechner, J.P. Amoureux, M. Bée and R. Fouret, *Commun. Phys.* **2**, 207 (1977).
- [64] M. Bée, J.P. Amoureux and R.E. Lechner, *Mol. Phys.* **4**, 945 (1980).
- [65] G. Cardini, R. Righini and S. Califano, *J. Chem. Phys.* **95**, 679 (1991).
- [66] W.S. Gornall and B.P. Stoicheff, *Phys. Rev.* **B4**, 4518 (1971).
- [67] H. Fontaine and C. Moriametz, *J. Chim. Phys.* **65**, 969 (1968).

